PAPER • OPEN ACCESS

A unified approach for the calculation of in-plane dielectric constant of films with interdigitated electrodes

View the article online for updates and enhancements.

A unified approach for the calculation of in-plane dielectric constant of films with interdigitated electrodes

Trygve M Reader[1] , **Ulrik Hanke**[2] , **Einar Halvorsen**[2] **and Tor Grande**[1]

[1] Department of Material Science and Engineering, NTNU Norwegian University of Science and Technology, Trondheim, Norway
[2] Department of Microsystems, USN University of South-Eastern Norway, Campus Vestfold, Horten, Norway

E-mail: trygvrad@gmail.com

CrossMark

Abstract

Interdigitated electrodes (IDEs) on dielectric films is an important electrode design in electrical components such as transducers and sensors. Further development and use of IDEs for characterization of the in-plane properties of dielectric films requires models for the capacitance, particularly when used in a multilayer stack. Previous models for the capacitance have permitted erroneous boundary conditions between layers with associated limitations to accuracy. In this work we present a new model based on fulfilling the boundary conditions between layers with different dielectric constant. We further demonstrate how the model can be used to calculate the in-plane dielectric constant and polarization of $BaTiO_3$ films. The model is shown to outperform previous models using both the experimental data from $BaTiO_3$ films on $SrTiO_3$ substrates and finite element method simulations of the corresponding case. One important advantage compared to previous work is that the new model provides good results regardless of film thickness.

Supplementary material for this article is available online

(Some figures may appear in colour only in the online journal)

1. Introduction

Interdigitated electrodes (IDEs) are the most used electrodes for exploring the in-plane properties of dielectric thin films. Accurate characterization of dielectric properties of thin films with IDEs is highly relevant for applications such as tunable capacitors [1–3] and chemical sensors [4–9] that rely on change in material properties due to external stimuli. For devices that utilize the piezoelectric effect, such as surface acoustic wave devices [10–12] and piezoelectric transducers [13, 14], the dielectric properties must be understood in order to describe the electric field and coupling to the piezoelectric effect.

A model describing the electric field is required to couple material properties to the capacitance of IDE devices. The electric field surrounding infinitely spanning IDEs sandwiched between two infinitely spanning materials was solved analytically by Engan [15], while several approaches have been used to estimate the capacitance of IDEs in combination with a thin film. Ponamgi [16] addressed the boundary condition between

different layers directly by generating additional potentials from the interface, and used this to generate a set of equations that could estimate the capacitance when solved by linear algebra. A similar approach of generating additional potentials, known as the method of recursive images, has recently been revisited by Diaz and Igreja [17], where unphysical boundary conditions at the interface with the electrode were used in order to preserve the potential at the electrodes. Wu *et al* [1] developed an alternate approach, known as the parallel partial capacitance (PPC) model, where the interfaces are instead ignored, and the structure is divided into partial structures and the capacitance of each partial structure is evaluated separately. Conformal mapping approaches of increasing accuracy were developed by Gevorgian *et al* [18] and Igreja and Dias [19]. However, improper treatment of boundary conditions still limits the accuracy of this approach [20, 21]. Moreover, other applications of IDEs may deviate from the basic design and include additional electrodes. This includes systems with electrodes both on top and below a thin film [22], or thin film with IDEs fabricated on a conducting substrate, where the substrate acts as a third electrode [13, 23]. The use of a conducting substrate was considered by Nguyen *et al* [24] as an additional contribution to the capacitance, but in general the inclusion of additional electrodes has not been addressed in the models previously described in literature.

Here, a numerical model for the capacitance of IDE structures in multilayer stacks is presented. The model is optimized to calculate the dielectric constant of a single layer on a substrate with known dielectric properties. Validation is provided by application of the model on experimental data for two $BaTiO_3$ films on a $SrTiO_3$ substrates combined with finite element method (FEM) simulations. $BaTiO_3$ was chosen as it is a prototype ferroelectric material with well-known properties. Finally, a Python implementation of the model is available on Github [25], including examples of use for a variety of geometries.

2. The model

2.1. Layout of IDEs

The layout of a set of IDEs in the *x-z* plane is shown in figure 1(a). The IDEs consist of two comb electrodes with a total of *N* fingers. The fingers with positive potential overlaps with the fingers with negative potential in a region of length *L* in the *z* direction. Here we assume that the ratio between the periodicity of the electrodes and *L* is such that fringe effects at the end of the fingers are negligible and can be ignored. A cross section of the structure (*x-y* plane) is shown in figure 1(b). The spacing between the electrodes, *a*, and the finger width, *b*, are indicated. The figure shows a general design with one layer of finite thickness (medium 2, with thickness t_2), between two layers of infinite thickness (medium 1 and medium 3).

For this work we describe the geometry by the cover fraction $\eta = b/(a+b)$ [19] and the normalized thickness of medium 2, $\tau_2 = t_2/(a+b)$. Normalizing the geometry also gives rise to the dimensionless coordinates $x' = x/(a+b)$ and $y' = y/(a+b)$.

The total capacitance of the structure can be estimated by considering the individual capacitance between each pair of fingers. Following the route of reference [19], we only consider edge effects at the outermost electrode pairs (capacitance per unit length C_E), while periodic boundary conditions are used when considering the interior electrodes (capacitance per unit length C_I). An equivalent circuit diagram is shown in figure 1(b), and the total capacitance of the structure can be estimated as follows:

$$C_{total} = L((N-3)C_I + 2C_E) \tag{1}$$

2.2. The capacitance of interior fingers

The potential in the case where the thickness of medium 2 reaches infinity (*i.e.* $t_2 \to \infty$) may be calculated as described by Engan [15], Wu *et al* [1], Wei [12], or Igreja and Dias [19]. We will use the subscript $_\infty$ to mark the capacitance per unit length, $C_{I\infty}$, and potential, $V_{I\infty}(x,y)$, for this case. The required expressions for calculating $C_{I\infty}$ and $V_{I\infty}(x,y)$ using both a conformal mapping approach [19] and a Fourier approach [15] are included in section 1 of the Supporting Information (stacks.iop.org/SMS/29/115039/mmedia).

Given a finite thickness of medium 2, as shown in figure 1(b), boundary conditions at the interface between medium 2 and medium 3 must be fulfilled. The same is true for the interface between medium 2 and 1 between the electrode fingers. Using the initial field $V_{I\infty}$ as a basis, we here use the method of recursive images to fulfil the boundary conditions between the layers [17]. This will distort the constant potential at the electrodes, and we will address this distortion later. In the method of recursive images, a forward and a reverse potential is generated whenever a potential interacts with the boundary conditions at an interface. These potentials are defined using the forward, $f_{ij} = \frac{2\varepsilon(i)}{\varepsilon(i)+\varepsilon(j)}$, and reverse, $r_{ij} = \frac{\varepsilon(i)-\varepsilon(j)}{\varepsilon(i)+\varepsilon(j)}$, coefficients for the respective interface defined by the dielectric constant $\varepsilon(i)$ and $\varepsilon(j)$ in medium *i* and *j* [16, 17]. A derivation of the coefficients from the boundary conditions is included in section 2 of the Supporting Information, where anisotropic materials are also considered. The three first generations of potentials in the method of recursive images are illustrated in figure 2(a)–(c). Equation (2) describes the sum of all partial potentials generated, $V_{I1}(x,y)$, and this potential is illustrated in figure 2(d), while figure 2(e) shows the potential along the interface with the electrodes.

$$V_{I1}(x,y) = \begin{cases} V_{I\infty}(x,y) + f_{21}r_{23}\sum_{m=0}^{\infty} \\ (r_{23}r_{21})^m V_{I\infty}(x,-y+2(m+1)t_2), & \text{for } y < 0 \\ V_{I\infty}(x,y) + \sum_{m=0}^{\infty}(r_{23}r_{21})^{(m+1)}V_{I\infty}(x,2(m+1)t_2+y) \\ +r_{23}^{m+1}r_{21}^m V_{I\infty}(x,2(m+1)t_2-y), & \text{for } 0 < y < t_2 \\ f_{23}\sum_{m=0}^{\infty}(r_{23}r_{21})^m V_{I\infty}(x,y+2mt_2), & \text{for } y > t_2 \end{cases} \tag{2}$$

The potential, $V_{I1}(x,y)$, and the associated capacitance, C_{I1}, are denoted with the subscript 1, as we will soon place them in the context of a series of similar potentials. It can be seen from
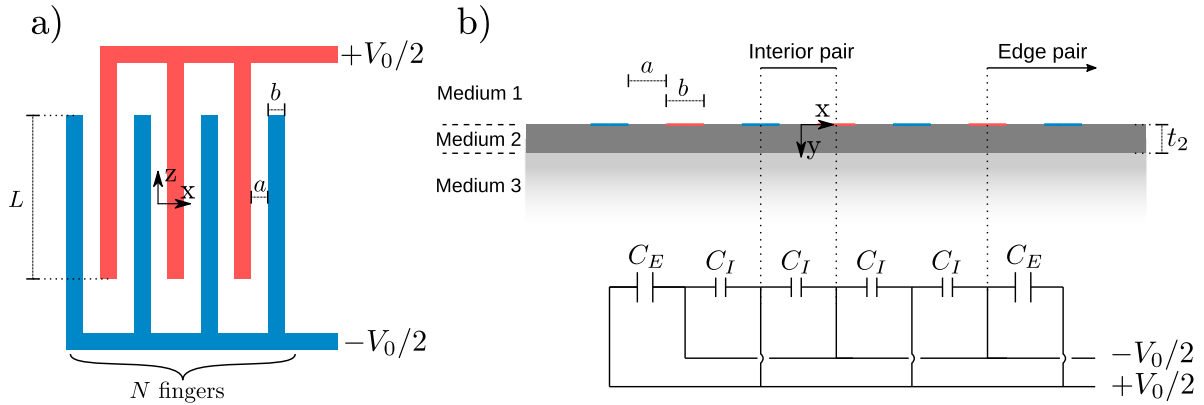
Figure 1. (a) Geometry of a set of interdigitated electrodes in the *x-z* plane. The finger overlap length *L* and number of fingers *N* are indicated. (b) A cross section of (a), showing the *x-y* plane. The electrode width *b*, electrode spacing *a*, and thickness of medium 2 (t_2), are indicated. An equivalent circuit model of the cross section is also shown. Each interior pair of electrodes is assumed to have capacitance per unit length C_I, while the edge pairs have a capacitance per unit length C_E.
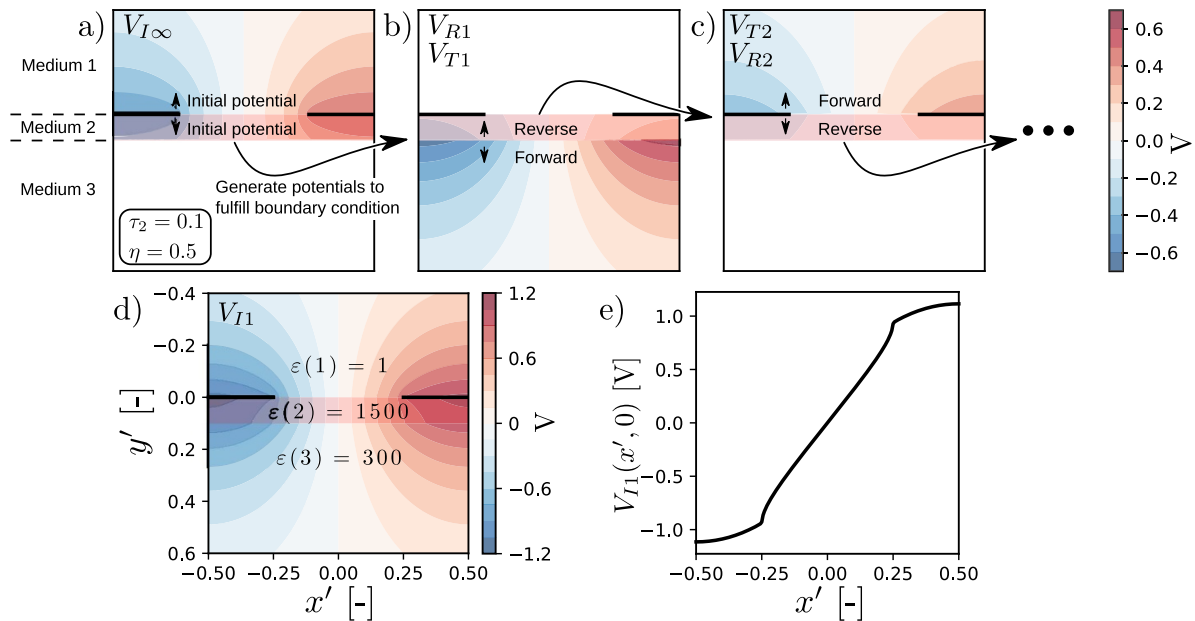

Figure 2. Method of recursive images. (a) The initial potential $V_\infty(x,y)$ is projected into medium 1 and 2. (b) The first reverse and forward potentials. (c) The reverse potential in (b) generates the set of reverse and forward potentials shown in (c). (d) The sum of the infinite series of reverse and forward potentials generated. (e) The total potential at the interface between material 1 and 2.

figure 2(d) and (e) that the potential $V_{I1}(x, y)$ does not respect boundary conditions (± 0.5 V) at the electrodes. The total displacement field in the *x* direction remains constant when using the method of recursive images, so that C_{I1} can be calculated using the expression for $C_{I\infty}$.

We now proceed to use linear algebra to address the non-constant potential at the electrodes. For this approach we generate a series of potentials V_{Ii} with ever decreasing cover fraction η_i with $i = 1...M$. Any linear combination of these potentials, will fulfil the boundary conditions at all interfaces with the exception of the electrodes, and we seek a linear

combination that will approximate correct boundary conditions also here. The combined potential $V_{Ic}(x, y)$ and capacitance C_{Ic} may be found if appropriate weights u_i are known:

$$V_{Ic}(x,y) = \sum_{i=1}^{M} u_i V_{Ii}(x,y) \tag{3}$$

$$C_{Ic} = \sum_{i=1}^{M} u_i C_{Ii} \tag{4}$$

The weights u_i may be found by using linear algebra to balance the potential at M locations along the electrode surface, denoted x_j with $j = 1...M$. A linear distribution of cover fractions η_i and locations x_j is chosen for simplicity, as detailed by equations (5) and 6:

$$\eta_i = \eta_1 \left(1 - \frac{i-1}{M} \right) \tag{5}$$

$$x_j = -\frac{1}{2} \left(a + b\frac{2j-1}{2M} \right) \tag{6}$$

Solving the linear algebra problem in equation (7) will then yield the weights u_i. Here V_0 is the potential applied to the electrodes, and is set to 1 V.

$$\begin{bmatrix} V_{I1}(x_1,0) & V_{I1}(x_2,0) & \dots & V_{I1}(x_M,0) \\ V_{I2}(x_1,0) & V_{I2}(x_2,0) & \dots & V_{I2}(x_M,0) \\ \dots & \dots & \dots & \dots \\ V_{IM}(x_1,0) & V_{IM}(x_2,0) & \dots & V_{IM}(x_M,0) \end{bmatrix} \dots \begin{bmatrix} u_1 \\ u_2 \\ \dots \\ u_M \end{bmatrix} = \begin{bmatrix} V_0/2 \\ V_0/2 \\ \dots \\ V_0/2 \end{bmatrix} \tag{7}$$

An example of the potential described by a linear combination of $M = 4$ components is shown in figure 3(a) and (b), while each of the 4 components are shown separately in figures 3(c)–(f). It can be clearly seen that $V_{Ic}(x, y)$ is in reasonable agreement with the boundary conditions that require $+0.5$ V at the left electrode and -0.5 V at the right electrode.

2.3. The in-plane polarization in a ferroelectric thin film

We here propose a method for estimating the average in-plane polarization in the film at the plane midway between the electrode fingers ($x = 0$). At this plane, the displacement field is parallel to the x-axis, and distributed between the film, substrate, and air. By estimating the sum of the displacement fields in the substrate and air using the proposed model, these can be subtracted from the charge collected by the electrodes in order to calculate the polarization in the film as given in equation (8). Here Q_{exp} is the experimentally collected charge at the electrodes, and Q_{sub} and Q_{air} are the integrated displacement fields in substrate and air, respectively. Q_{sub} and Q_{air} can be calculated based on the potential given by equation (3) by approximating the film as a homogeneous non-ferroelectric material. The details for calculating Q_{sub} and Q_{air} are provided in section 3 of the Supporting Information. The polarization, P, is may then be calculated according to equation (8):

$$P = \frac{Q_{\mathrm{exp}} - Q_{\mathrm{air}} - Q_{sub}}{t_2 L(N-1)} \tag{8}$$

2.4. Capacitance of the edge pair

The capacitance of an exterior pair of electrodes was approximated by Igreja and Dias [19] by assuming a plane of constant potential at the center of the outermost electrode gap, and with no flux passing the plane at the center of the next-to-outermost electrode. Using these approximations, the edge capacitance

can be calculated as follows:

$$C_{Ec} = \frac{2C_{2c}C_{Ic}}{C_{Ic} + C_{2c}} \tag{9}$$

where the subscript 2 denotes a set of IDEs with only two electrode fingers. Equations (2), 7 and 4 may easily be adapted to calculate C_{2c} using the initial potential $V_{2\infty}(x, y)$, as detailed in section 4 of the Supporting Information.

2.5. Multiple sets of electrodes

The linear algebra approach in equation (7) may be expanded to include additional electrodes at different interfaces in a multilayer stack, and the implementation of this model available on Github is to handle any number of layers with an arbitrary number of electrodes [25]. This may for example be interdigitated electrodes on top of one or more thin films grown on a conducting substrate, where the substrate acts as a separate electrode [13, 23], or alternatively systems with electrodes on both sides of a film [22]. The potential of such systems are illustrated in section 5 of the Supporting Information.

2.6. Anisotropic materials

Anisotropic materials may be addressed by transforming the potential as $y \rightarrow \varepsilon_r y$, where $\varepsilon_r = \sqrt{\frac{\varepsilon_x}{\varepsilon_y}}$ [12, 15], and adapting the boundary conditions appropriately [16]. The code on Github is designed to support this while the constituent equations required are included in section 2 of the Supporting Information.

3. Experimental

Two (100) oriented BaTiO$_3$ films 47.4$\pm$ 1.1 nm and 142.2$\pm$ 1.0 nm thick deposited on (100) SrTiO$_3$ substrates ($10\times$ $10\times$ 0.5 mm, Crystal GmbH, Berlin, Germany) were fabricated to obtain experimental data for the validation of the model. The films were prepared by a chemical solution deposition prosess reported elsewhere [26]. The (100) BaTiO$_3$ films are under tensile strain due to the mismatch in thermal expansion between SrTiO$_3$ and BaTiO$_3$ [26], and this is suggested to give an a_1/a_2 domain pattern, which has recently been confirmed [27]. The mismatch between the lattice parameter of the substrate and film is relaxed by lattice dislocations at the interface [28]. The thickness of each film was measured by transmission electron microscopy, with images included in section 6 of the Supporting Information.

The electrodes were deposited using lift-off and e-beam evaportaion of 5 nm Ti and 20 nm Pt [26]. Six sets of IDEs, each with a $1\times$ 1 mm footprint, were patterned on each of the two films, with the fingers aligned along the [010] pseudocubic axis of the film. The finger spacings (a) varied from 3 to 15 μm and the finger width (b) varied in the range 1.5 to 3.2 μm. The electrode widths and gaps were measured using an automated image analysis procedure and the uncertainty in the widths was $\pm$ 80 nm. The geometries of the IDEs are tabulated in section 7 of the Supporting Information.
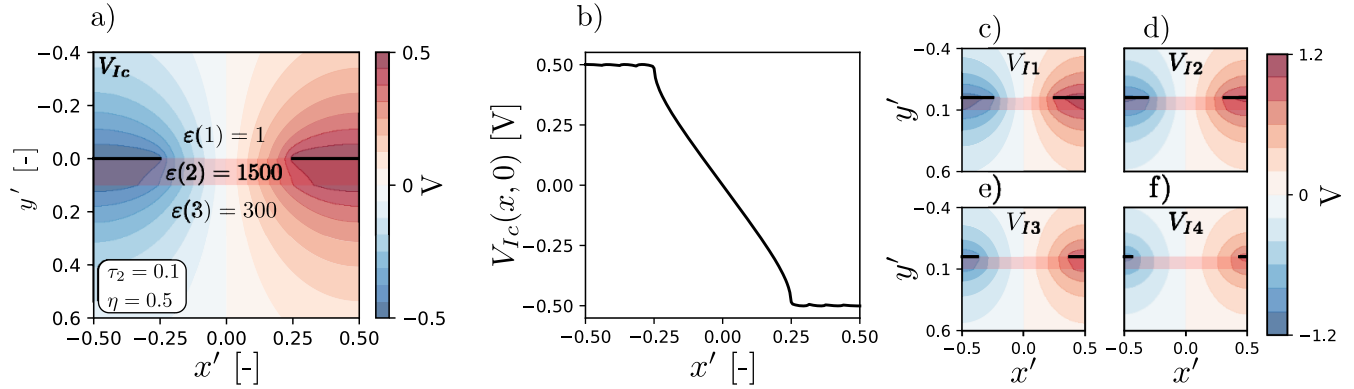
Figure 3. Example of potential using the proposed model with 4 components. (a) The combined potential using four components. (b) the potential along the interface with the electrodes. (c)–(f) The potential of the four components used for the combined potential in (a).

Electrical characterization at 1 kHz was performed using an Aixacct TF2000 thin film analyser with a ceramic thin-film sample holder (aixACCT Systems GmbH, Aachen, Germany). The small signal voltage was varied so that the corresponding characteristic in-plane electric field, $E_{\text{characteristic}}$, in the film between the electrode fingers was 0.2 kV cm^{-1}, calculated by as follows [24]:

$$E_{\text{characteristic}} = \frac{V}{a + 4\ln(2)t_2/\pi} \quad (10)$$

where V is the applied voltage. A bias sweep was performed with a frequency of 0.1 Hz and an amplitude of 20 kV cm^{-1}. The dielectric constant of the SrTiO$_3$ substrate was determined to be 317± 1.2, based on measurements from IDEs on a pure SrTiO$_3$ substrate (not shown). The dielectric constant of the substrate was found to be independent of the applied voltage in the range relevant for this study. Charge-potential hysteresis loops were captured at 30 Hz.

$M = 16$ components were used for the model when determining the dielectric constant of the film from the experimental capacitance. Both the film and substrate were treated as isotropic in the verification of the model.

3.1. Finite element method (FEM) simulations

The FEM simulations were performed using the FEMM software [29]. For calculating the interior capacitance, $C_{I,FEM}$, a cell was made with dimensions $(a+b) \times 4(a+b)$ and with Neumann boundary conditions (zero flux) on all outside boundaries. For the vertical boundaries this is equivalent to a periodic boundary condition. The limited height of the cell reduces the accuracy, but with the height used here the reduction in accuracy was not found to be significant. The grid density was varied depending on τ_2, as thinner films require higher grid density to obtain sufficient accuracy. Up to 1 million nodes were used for the simulations. By assuming that the capacitance calculated by FEM is accurate, we can evaluate the accuracy of the model presented here as follows:

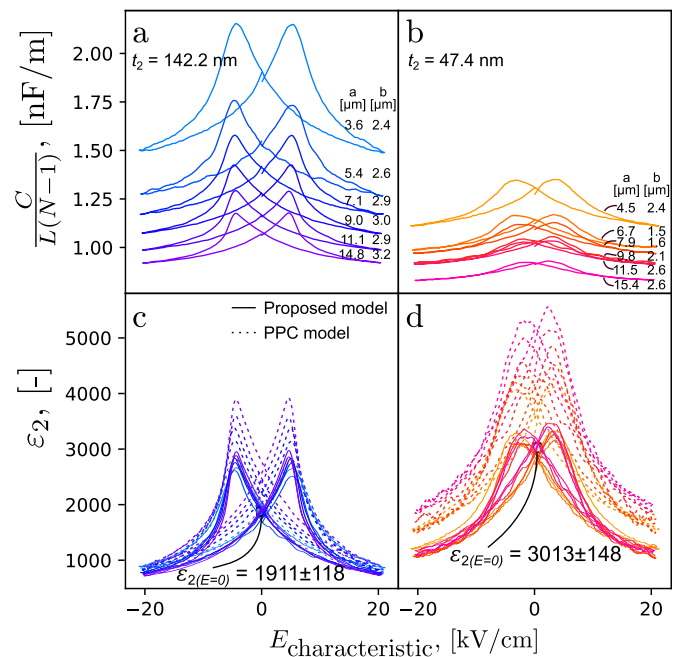$$\text{Accuracy} = 100\% \frac{C_{Ic}}{C_{I,FEM}} \quad (11)$$

Figure 4. The capacitance of the BaTiO$_3$ films with thickness (t_2) of 142 nm (a) and 47 nm (b). The capacitance is normalized with respect to the finger length L and number of fingers gaps ($N-1$). The calculated dielectric constant, ε_2, as function of applied bias of the BaTiO$_3$ films with thickness 142 nm (c) and 47 nm (d). The value at zero field is indicated for both films.

4. Results

4.1. Application of the model to BaTiO$_3$ films on SrTiO$_3$ substrates

The capacitances measured using geometrically different IDEs on the two films are shown in figure 4(a) and (b), where the capacitance has been normalized with respect to the number of gaps and the finger length. Based on the capacitance data, the dielectric constant was calculated using the model and the resulting dielectric constant-electric field, $\varepsilon(2)$–E, loops are shown in figure 4(c) and (d). The relative dielectric constant in the BaTiO$_3$ films at zero field is 1911±
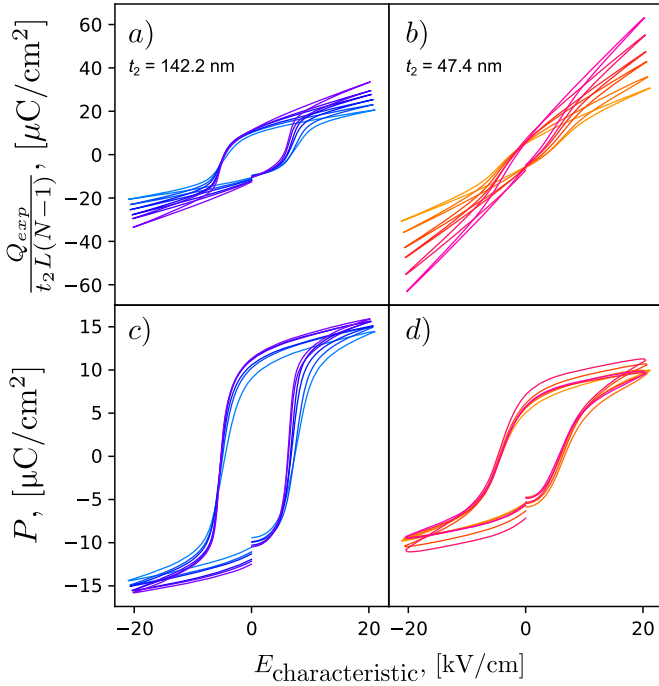
Figure 5. The collected charge at the electrodes of the BaTiO$_3$ films with thicknesses, t_2, of 142 nm (a) and 47 nm (b). The charge is normalized with respect to the film thickness t_2, finger length L and number of fingers gaps $(N - 1)$. The polarization calculated using equation (8) of the BaTiO$_3$ films with thickness 142 nm (c) and 47 nm (d).
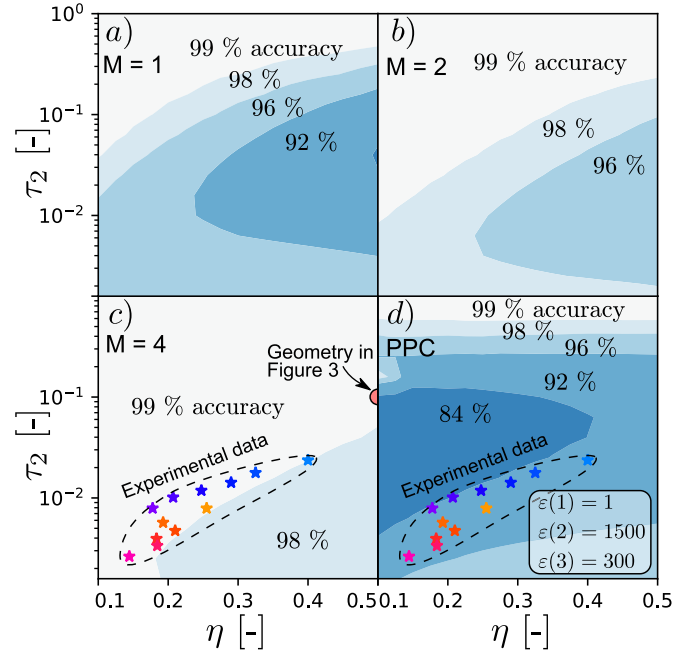

Figure 6. The accuracy (equation (11)) of the model when compared to FEM as a function of τ_2 and η for $M = 1$ (a), $M = 2$ (b) and $M = 4$ (c). The stars in (c) and (d) mark the geometries used for the experimental data presented in figure 4, while the circle in (c) marks the geometry shown in figure 3. (d) Accuracy of the PPC model when compared to FEM.

118, and 3013 ± 148 for the thick and thin film, respectively. The dielectric constant as calculated using the PPC model is shown for comparison. The constituent equations of the PPC model are included in section 8 of the Supporting Information [19].

A sensitivity analysis of the calculated dielectric constant with respect to the geometric parameters is included in section 9 of the Supporting information. Given the uncertainty of the geometric parameters, an uncertainty of ∼ 100 is expected for the dielectric constant of the thick film. The sensitivity analysis also examined the impact of anisotropy in the dielectric constant of the film, and it was found that the capacitance has much higher sensitivity to the in-plane component than the out-of-plane component.

Capacitance curves generated by the model using the field-dependent permittivity of figures 4(c) and (d) are presented in section 10 of the Supporting Information. The calculated capacitance curves represent a good fit to the experimental curves.

The charge collected at the electrodes when performing a voltage sweep is shown in figure 5(a) and (b) for the thick and thin films, respectively. A large capacitive contribution from the substrate can be seen in the slope of the curves. Figure 5(c) and (d) shows the polarization in the BaTiO$_3$ films as calculated by equation (8), where the contributions from the substrate and air have been subtracted using the model. The remnant polarization was found to be 10.54± 0.87 μC cm^{-2} and 5.75± 0.67 μC cm^{-2} for the thick and thin films, respectively, while the coercive field was 5.88± 0.14 kV cm^{-1} and 5.48± 0.21 kV cm^{-1}.

4.2. Evaluation of the model by FEM

The accuracy of the model compared to FEM (equation (11)) for a structure with an infinite number of fingers (C_{Ic}) is shown in figures 6(a)–(c) using a varying number of components M. The accuracy of the PPC model is shown in figure 6(d) for comparison. The accuracy of the proposed model is maximum when considering a thick film with a low cover fraction. When a single component is used, the accuracy is higher or comparable to that of the PPC model for the entire region probed. The accuracy increases with increasing number of components. When using $M = 4$ components, the model has more than 99 % accuracy for the geometries used to obtain the experimental data in figures 4 and 5. The PPC model has an accuracy greater than 92 % for the same geometries, a difference of 7 percentage points. The relative uncertainty of the FEM simulations used to compare the models is estimated to be 0.1 % based on the finite grid density and simulated cell height.

5. Discussion

IDEs with different geometrical dimensions deposited the two BaTiO$_3$ films formed the basis for experimental verification of the model. The hysteresis loops for the different IDE geometries, shown in figure 4 and 5, are superimposed on each other. The data shown in figures 4(c) and (d) clearly demonstrate that the model gives a consistent field-dependent capacitance for both the thick and thin films. Moreover, the polarization-electric field hysteresis loops, shown in figures 5(c) and (d), show that we can also calculate the polarization versus electric

field. However, equation (7) used to calculate polarization are based on several approximations, and a more accurate equation for the polarization can be further developed. Finally, the two films do not have the same electrical properties, which we will return to in the end of this section.

The dielectric constant of $BaTiO_3$ is anisotropic [30], and crystallographically textured $BaTiO_3$ films are therefore anisotropic in nature [31], but the sensitivity analysis (section 9, Supporting Information) demonstrates that the out-of-plane component of the dielectric constant of the two $BaTiO_3$ films has only a minor effect on the measured capacitance of the system investigated here. The error due to neglection of the anisotropic contribution is therefore low. The low sensitivity to the out-of-plane component is related to the high ratio between the electrode spacing and film thickness used for this study (low τ_2), which results in a homogenous in-plane electric field in the $BaTiO_3$ films between the electrode fingers. Furthermore, the low sensitivity to the out-of-plane component implies that the (isotropic) dielectric constant found here can be treated as an approximation of the in-plane component of the dielectric constant in the film.

The model developed here outperforms the PPC model as evident by the lower distribution in the calculated dielectric constant (figures 4(c) and (d)). A similar trend is observed when the two models are compared to results from FEM, where the model outperforms the PPC model for both periodic structures (figure 6), and when considering structures with a limited number of fingers (section 11 of the Supporting Information). For an anisotropic film, a validation by FEM is included together with the constituent equations in section 2 of the Supporting Information.

The electrodes were oriented along the [010] direction so that the electric field was applied primarily along the [100] in-plane direction of the $BaTiO_3$ films. The films have an a_1/a_2 in-plane domain pattern, with the polar axis alternating between the [010] and [100] in-plane directions [26]. The observed dielectric constants of the films are within the range observed for $BaTiO_3$ single crystals with 4000 along the polar axis and 200 orthogonal to the polar axis [30], while the remnant polarization is lower than that of single crystals (26 μC cm^{-1}) [32]. The intermediate dielectric constant and lower polarization when compared to single crystal $BaTiO_3$ is expected, considering the proposed a_1/a_2 domain pattern. The remnant polarization is comparable to what has recently been achieved in-plane for a 80 nm $BaTiO_3$ films grown by pulsed laser deposition on $NdScO_3$ (12 μC cm^{-1}) [33]. The dielectric constant and remnant polarization are calculated by assuming a homogeneous film. However, the epitaxial coupling with the substrate will yield compressive strain at the interface [34], while away from this interface the film is relaxed by edge dislocations and will experience tensile strain due to a difference in the thermal expansion coefficient [26]. The in-plane properties depend on the strain state, where compressive strain favours a high in-plane dielectric constant, and tensile strain favours high in-plane polarization [31]. The film properties obtained by assuming a homogeneous film are therefore expected to be thickness dependent. For the two films examined here, a lower average polarization and a higher

dielectric constant are found for the thinner film, consistent with the suggested inhomogeneity.

The effect of piezoelectricity has not been considered for this work. The piezoelectric effect impacts the anisotropy in the dielectric constant, as the films are clamped in the in-plane directions, but free to move in the out-of-plane direction. Thus, the dielectric constant is expected to correspond to the effective permittivity for a film with interdigitated electrodes. Equations of state for such films were discussed in [35].

6. Conclusion

A new model for the capacitance and potential of IDEs was presented and it was shown that the new model was more accurate than the PPC model both when applied to experimental data, and when compared to FEM. The model is applicable for more geometries, such as systems where a conducting substrate is used as a support for a multilayer stack with IDEs, or where one or more layers have an anisotropic dielectric constant. Furthermore, a method for calculating the in-plane polarization of a ferroelectric film has been demonstrated using the proposed model. A full implementation of the model is available on Github, including examples for a variety of geometries.

ORCID iDs

Trygve M Reader ⬤ https://orcid.org/0000-0003-3524-362X
Ulrik Hanke ⬤ https://orcid.org/0000-0001-9470-767X
Einar Halvorsen ⬤ https://orcid.org/0000-0001-6511-9190
Tor Grande ⬤ https://orcid.org/0000-0002-2709-1219

References

[1] Wu H-D, Zhang Z, Barnes F, Jackson C M, Kain A and Cuchiaro J D 1994 Voltage tunable capacitors using high temperature superconductors and ferroelectrics *IEEE Trans. Appl. Supercond.* **4** 156–60

[2] Al-Shareef H N, Dimos D, Raymond M V, Schwartz R W and Mueller C H 1997 Tunability and calculation of the dielectric constant of capacitor structures with interdigital electrodes *J. Electroceramics* **1** 145–53

[3] Meyers C J G, Freeze C, Stemmer S, Lan X, Chau L and York R A 2016 Two-port tunable interdigital capacitors fabricated on low-loss MBE-grown $Ba_{0.29}Sr_{0.71}TiO_3$ 1-4 2016 IEEE MTT-S International Microwave Symposium (IMS) San Francisco

[4] Zaretsky M C, Melcher J R and Cooke C M 1989 Moisture sensing in transformer oil using thin-film microdielectrometry *IEEE Trans. Electr. Insul.* **24** 1167–76

[5] Qu W and Wlodarski W 2000 A thin-film sensing element for ozone, humidity and temperature *Sensors Actuators* B **64** 42–8

[6] Hagleitner C, Hierlemann A, Lange D, Kummer A, Kerness N, Brand O and Baltes H 2001 Smart single-chip gas sensor microsystem *Nature* **414** 293–6

[7] Casalini R, Kilitziraki M, Wood D and Petty M C 1999 Sensitivity of the electrical admittance of a polysiloxane film to organic vapours *Sensors Actuators* B **56** 37–44

[8] Endres H E and Drost S 1991 Optimization of the geometry of gas-sensitive interdigital capacitors *Sensors Actuators* B **4** 95–8

[9] Zhou R, Hierlemann A, Weimar U and Göpel W 1996 Gravimetric, dielectric and calorimetric methods for the detection of organic solvent vapours using poly(ether urethane) coatings *Sensors Actuators* B **34** 356–60

[10] Ruppel C C W 2017 Acoustic wave filter technology-A review *IEEE Trans. Ultrason. Ferroelectr. Freq. Control* **64** 1390–400

[11] Bo L, Xiao C, Hualin C, Ali Mohammad M, Xiangguang T, Luqi T, Yi Y and Tianling R 2016 Surface acoustic wave devices for sensor applications *J. Semicond.* **37** 021001

[12] Wei J S 1977 Distributed capacitance of and acoustic surfac *IEEE J. Quantum Electron.* **13** 152–8

[13] Hong E, Trolier-McKinstry S, Smith R L, Krishnaswamy S V and Freidhoff C B 2006 Design of MEMS PZT circular diaphragm actuators to generate large deflections *J. Microelectromech. Syst.* **15** 832–9

[14] Chidambaram N, Balma D, Nigon R, Mazzalai A, Matloub R, Sandu C S and Muralt P 2015 Converse mode piezoelectric coefficient for lead zirconate titanate thin film with interdigitated electrode *J. Micromech. Microeng.* **25** 045016

[15] Engan H 1969 Excitation of elastic surface waves by spatial harmonics of interdigital transducers *IEEE Trans. Electron Devices* **16** 1014–17

[16] Ponamgi S R and Tuan H-S 1974 Theoretical calculation of capacitance of an IDT over a piezoelectric layered structure *IEEE Trans. Sonics Ultrason.* **21** 125–7

[17] Dias C J and Igreja R 2017 A method of recursive images to obtain the potential, the electric field and capacitance in multi-layer interdigitated electrode (IDE) sensors *Sensors Actuators* A **256** 95–106

[18] Gevorgian S S, Martinsson T, Linnér P L J and Kollberg E L 1996 CAD models for multilayered substrate interdigital capacitors *IEEE Trans. Microw. Theory Tech.* **44** 896–904

[19] Igreja R and Dias C J 2004 Analytical evaluation of the interdigital electrodes capacitance for a multi-layered structure *Sensors and Actuators* A **112** 291–301

[20] Ghione G and Goano M 2003 Revisiting the partial-capacitance approach to the analysis of coplanar transmission lines on multilayered substrates *IEEE Trans. Microw. Theory Tech.* **51** 2007–14

[21] Vukadinovic M, Malic B, Kosec M and Krizaj D 2009 Modelling and characterization of thin film planar capacitors: Inherent errors and limits of applicability of partial capacitance methods *Meas. Sci. Technol.* **20** 115106

[22] Williams R B, Park G, Inman D J and Wilkie W K 2002 An overview of composite actuators with piezoelectric fibers *20th International Modal Analysis Conference* Los Angeles pp 1–7

[23] Nigon R, Raeder T M and Muralt P 2017 Characterization methodology for lead zirconate titanate thin films with interdigitated electrode structures *J. Appl. Phys.* **121** 204101

[24] Nguyen C H, Nigon R, Raeder T M, Hanke U, Halvorsen E and Muralt P 2018 Probing-models for interdigitated electrode systems with ferroelectric thin films *J. Phys. D: Appl. Phys.* **51** 175303

[25] Ræder T M Interdigitated electrodes 2020 https://doi.org/10.5281/zenodo.4020684

[26] Raeder T M, Bakken K, Glaum J, Einarsrud M A and Grande T 2018 Enhanced in-plane ferroelectricity in BaTiO$_3$ thin films fabricated by aqueous chemical solution deposition *AIP Adv.* **8** 105228

[27] Raeder T M, Holstad T, Nylund I-E, Einarsrud M-A, Glaum J, Meier D and Grande T 2020 *Manuscript in preparation*

[28] Suzuki T, Nishi Y and Fujimoto M 1999 Analysis of misfit relaxation in heteroepitaxial BaTiO$_3$ thin films *Phil. Mag.* A **79** 2461–83

[29] Meeker D 2010 Finite element method magnetics www.femm.info Acccessed: 2019

[30] Merz W J 1949 The electric and optical behavior of BaTiO$_3$ single-domain crystals *Phys. Rev.* **76** 1221–5

[31] Waser R, Pertsev N A and Koukhar V G 2001 Thermodynamic theory of epitaxial ferroelectric thin films with dense domain structures *Phys. Rev.* B **64** 1–15

[32] Choi K J 2004 Enhancement of Ferroelectricity in Strained BaTiO$_3$ Thin Films *Science* **306** 1005–9

[33] Everhardt A S *et al* 2020 Temperature-independent giant dielectric response in transitional BaTiO$_3$ thin films *Appl. Phys. Rev.* **7** 011402

[34] Sun H P, Tian W, Pan X Q, Haeni J H and Schlom D G 2004 Evolution of dislocation arrays in epitaxial BaTiO$_3$ thin films grown on (100) SrTiO$_3$ *Appl. Phys. Lett.* **84** 3298–300

[35] Muralt P 2008 Recent progress in materials issues for piezoelectric MEMS *J. Am. Ceram. Soc.* **91** 1385–96